Additive Manufacturing 29 (2019) 100811

Contents lists available at ScienceDirect

Additive Manufacturing

journal homepage: www.elsevier.com/locate/addma

Full length article

3D printing using powder melt extrusion

Bret M. Boyle[1], Panupoan T. Xiong[1], Tara E. Mensch, Timothy J. Werder, Garret M. Miyake*

Department of Chemistry, Colorado State University, Fort Collins, CO, United States

ARTICLE INFO

Keywords:
Additive manufacturing
3D printing
Extrusion

ABSTRACT

Additive manufacturing promises to revolutionize manufacturing industries. However, 3D printing of novel build materials is currently limited by constraints inherent to printer designs. In this work, a bench-top powder melt extrusion (PME) 3D printer head was designed and fabricated to print parts directly from powder-based materials rather than filament. The final design of the PME printer head evolved from the Rich Rap Universal Pellet Extruder (RRUPE) design and was realized through an iterative approach. The PME printer was made possible by modifications to the funnel shape, pressure applied to the extrudate by the auger, and hot end structure. Through comparison of parts printed with the PME printer with those from a commercially available fused filament fabrication (FFF) 3D printer using common thermoplastics poly(lactide) (PLA), high impact poly (styrene) (HIPS), and acrylonitrile butadiene styrene (ABS) powders (< 1 mm in diameter), evaluation of the printer performance was performed. For each build material, the PME printed objects show comparable viscoelastic properties by dynamic mechanical analysis (DMA) to those of the FFF objects. However, due to a significant difference in printer resolution between PME (X–Y resolution of 0.8 mm and a Z-layer height calibrated to 0.1 mm) and FFF (X–Y resolution of 0.4 mm and a Z-layer height of 0.18 mm), as well as, an inherently more inconsistent feed of build material for PME than FFF, the resulting print quality, determined by a dimensional analysis and surface roughness comparisons, of the PME printed objects was lower than that of the FFF printed parts based on the print layer uniformity and structure. Further, due to the poorer print resolution and inherent inconsistent build material feed of the PME, the bulk tensile strength and Young's moduli of the objects printed by PME were lower and more inconsistent (49.2 ± 10.7 MPa and 1620 ± 375 MPa, respectively) than those of FFF printed objects (57.7 ± 2.31 MPa and 2160 ± 179 MPa, respectively). Nevertheless, PME print methods promise an opportunity to provide a platform on which it is possible to rapidly prototype a myriad of thermoplastic materials for 3D printing.

1. Introduction

Extrusion-based 3D printing is among the most widespread additive manufacturing techniques, with users spanning from hobbyists to industrial manufacturing companies [1–5]. The widespread adoption of extrusion-based 3D printing can be largely attributed to the low-cost and straightforward method of printing compared to other printing techniques (e.g. stereolithography, laser sintering, polymer jetting, etc.) [6–10]. Application of extrusion-based 3D printing techniques have enabled the rapid and customized production of 3D objects, ranging for example from art to coatings to force-sensing technologies [11–14]. A common extrusion-based additive manufacturing method is fused filament fabrication (FFF), in which a thermoplastic filament is heated and passed through a printer head to create a 3D printed object by layering the extrudate in specified shapes [15–18]. The materials compatible with FFF are mostly thermoplastics that are typically processed into filament and spooled for use in FFF. Unfortunately, evaluating the capability of a novel material to be printed by FFF can be challenging due to the difficulty of precision filament processing, even with specialized equipment. As such, the ability to extrude materials not in filament form could facilitate a more efficient method to screen novel materials for 3D printing and increase the build material landscape of 3D printing bypassing the filament-processing step of FFF.

The application of novel build materials for additive manufacturing [19–22] has the potential to transform the current landscape of 3D printing technology since the properties of the material inputs will dictate the optical, thermal, and mechanical properties of the final printed object. Recent developments in build materials have enabled the production of printed objects with tailored optical, thermal, electrical, mechanical, and chemical properties [23–27]. However, the

* Corresponding author.
E-mail address: garret.miyake@colostate.edu (G.M. Miyake).
[1] Co-first authorship

https://doi.org/10.1016/j.addma.2019.100811
Received 5 May 2019; Received in revised form 12 July 2019; Accepted 28 July 2019
Available online 06 August 2019
2214-8604/ Published by Elsevier B.V.

adoption of these novel 3D printable materials has been slow due to the high cost and the requirement for pre-processing the raw materials into filament or pellets. To date, the two foremost examples of extrusion-based 3D printing from a pellet feedstock rather than a filament feedstock, have been demonstrated by big area additive manufacturing (BAAM) techniques [28–30] and Titan Robotics' Atlas printer series [31]. Titan's Atlas printer series can be modified to print production scale projects from thermoplastic pellets, and contains a build volume of 30″ x 30″ x 45″. However, the industrial scale of the BAAM techniques and the Atlas printers is not conducive to laboratory scale use. Thus, bench-top pellet extruders capable of printing less material have been fabricated such as, Direct3D [32] and the Rich Rap Universal Pellet Extruder (RRUPE) [33]. Although these two pellet extruders expand the variety of materials that can be printed [34] and are capable of printing smaller parts (on the order of 200 mm^3 or less), they are not designed for 3D printing of material feedstock that is not pre-processed into the form of pellets. This limitation of pellet extruders further restricts which thermoplastic materials can be 3D printed and presents an obstacle to printing non-processed novel material feedstock. Rather than requiring new materials to be printed by the FFF or pellet extrusion techniques, the ability to print directly from powder granules makes the process of 3D printing novel materials more accessible by reducing the need for specialized equipment beyond a printer head.

Here, we report a bench-top PME printer that was fabricated through modification of the Rich Rap Universal Pellet Extruder (RRUPE) design [33] and tested with powders (particle size range of 0.038 mm–1 mm in diameter) of common 3D printing thermoplastics, including poly(lactide) (PLA), high impact poly(styrene) (HIPS), and acrylonitrile butadiene styrene (ABS) (Figure S8, S9, and S10). The sources of each of these thermoplastic powders were mechanically ground FFF printed parts. The parts being ground were often defective parts that would have been disposed of, normally. The resulting PME prints were compared to FFF prints based on print quality, print resolution, material viscoelasticity, and bulk material tensile properties to determine the initial viability of the PME 3D printing technique.

2. Printer head design and modifications

Development of a 3D printer that can directly use a thermoplastic powder build material requires an understanding of the fundamental relationships between the printer head design and printer performance. Therefore, the design of the printer head is the major focus of the current study as it is critical to the success of printing 3D objects directly from powder. Analysis of current printer heads (e.g. RRUPE) designed to print pellets (particle sizes ˜ 3–5 mm in diameter) inspired us to iteratively design and optimize a bench-top PME printer head. The resulting PME printer (Fig. 1) can successfully print 3D objects, which establishes a 3D printing platform that reduces the time needed for pre-processing build materials and allows researchers the potential to rapidly prototype novel build materials.

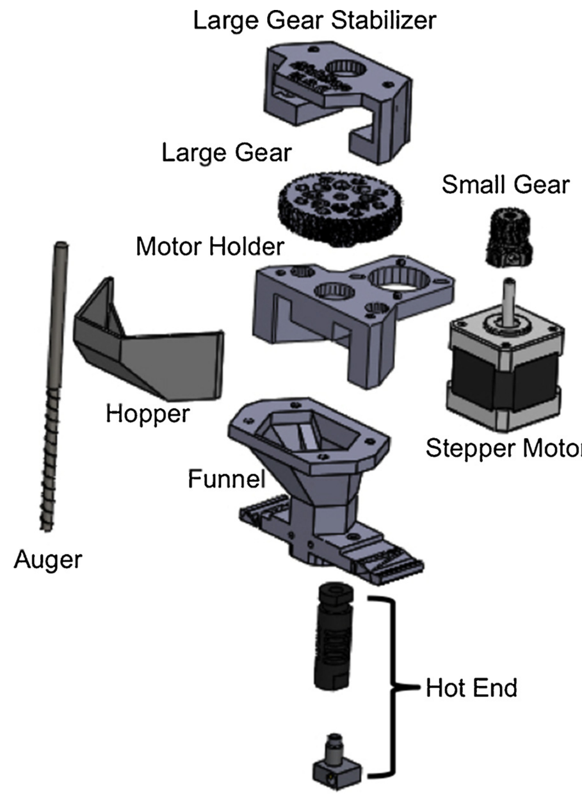

Fig. 2. Diagram of an exploded assembly model of the RRUPE design.

2.1. PME printer head design

An open-source, customizable printer, the MPCNC [35], was obtained to provide the control and axes needed to move the printer head. The printer was controlled electronically and with software as shown in Figures S1 and S2.The ability of the RRUPE printer head design was then investigated for powder extrusion since most of the components can be 3D printed by FFF and readily retrofitted to the MPCNC printer, enabling design optimization (Fig. 2). Starting at the closest part to the build plate, the brass nozzle (nozzle diameter = 0.4 mm) is connected to a polyether ether ketone (PEEK) tube, which comprises the commercially available Reifsnyder Precision Works hot end (RPWHE) [36]. The printer-head funnel then supports the hot end and is responsible for directing the build material to the auger. Above the entrance to the funnel, the build material resides in the hopper before it is directed into the funnel. The auger passes through the funnel from the top of the hot end to a large gear. The large gear is spun in a counterclockwise rotation by the smaller gear attached to the NEMA 17 stepper motor (0.48 N-m) to feed material from the funnel into the hot end.

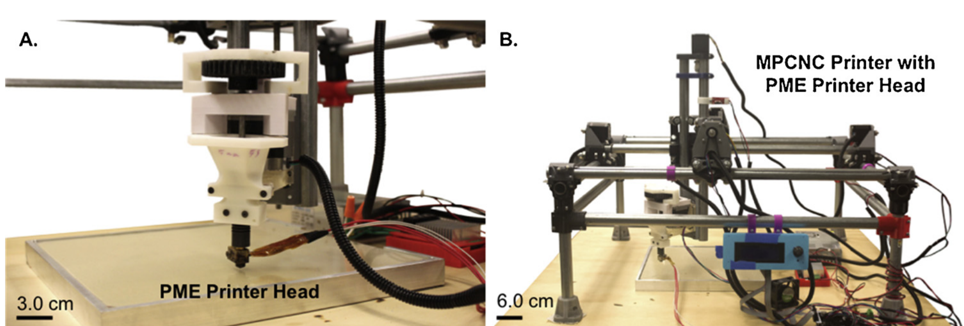

Fig. 1. Photographs of the final PME printer head (A.) and the PME printer head assembled on the open-source MPCNC printer (B.).

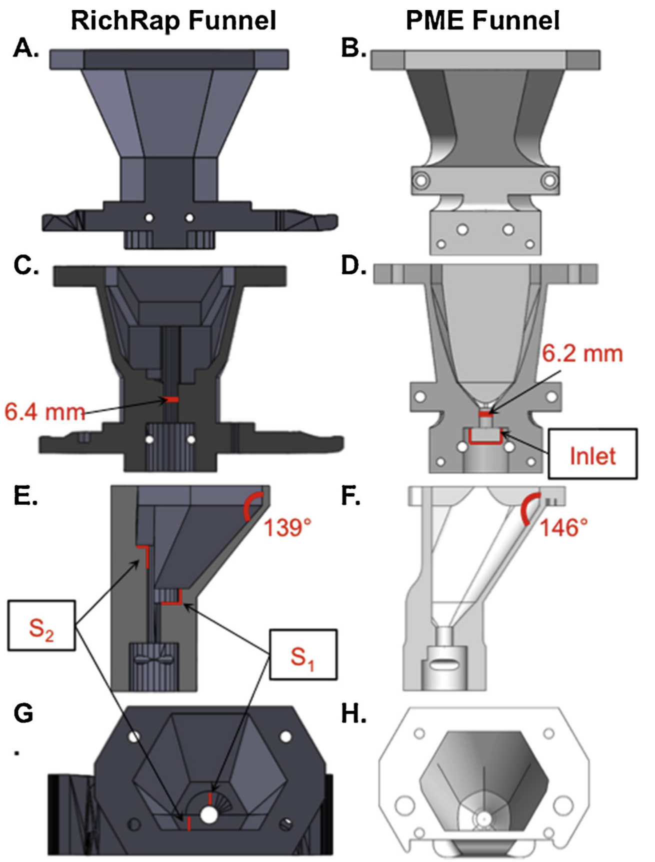

Fig. 3. The funnel design computer models of RichRap (A.) and PME (B.) with cross-sectional views from the front face (RichRap, C. and PME, D.) as well as the side profile cross-sectional views (RichRap, E. and PME, F.). The top-down view of the RichRap (G.) and PME (H.) funnels is shown.

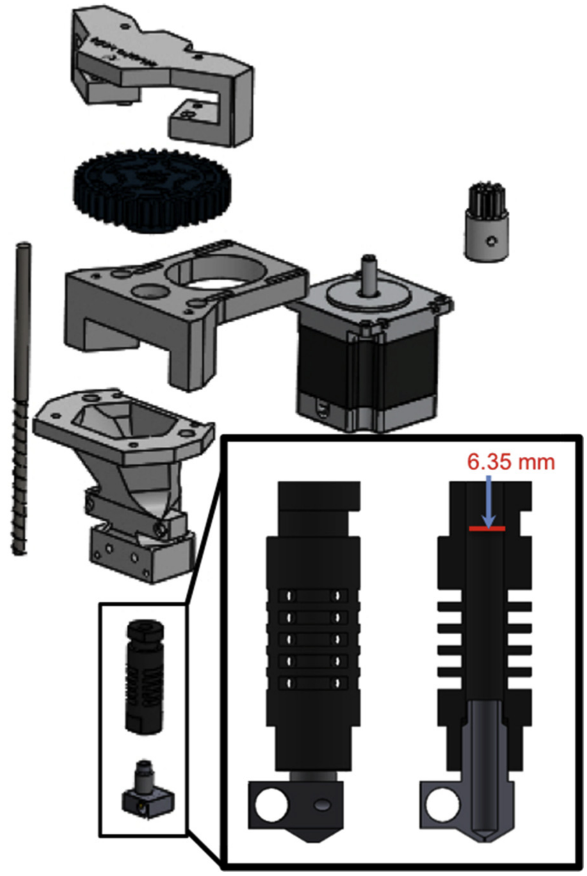

Fig. 4. A diagram of the exploded assembly computer model of the PME printer head with the RPWHE (inset shows a closer look at the RPWHE with a cross-sectional view).

2.2. RRUPE funnel modifications for PME

Extrusion with the RRUPE design was evaluated using a powdered poly(lactide) (PLA) build material ($<$ 1 mm in diameter, see Materials and Methods section and Figure S8 in Supporting Information for additional details), however, no extrusion of the PLA build material was observed. An analysis of the RRUPE printer head (Fig. 3) after a PLA powder extrusion attempt revealed that the funnel was not delivering powder to the hot end. To address this limitation, the funnel geometry was redesigned in 3-steps (Fig. 3): (**1**) the angle of the funnel was increased from 139° in the RichRap funnel (Fig. 3E) to 146° in the PME funnel (Fig. 3F) to better match the helix angle of the auger (typically 24° – 32°) with the supplementary angle of the funnel which would facilitate powder delivery to the auger without over-filling and clogging the auger; (**2**) the sharp angles in the interior of the funnel were replaced with fillets (top-down view of the two funnels in Figs. 3G and 3 H), which reduce the boundaries and points of friction that the powder experiences while traveling to the auger, and; (**3**) the two shelf cutouts (S_1, S_2) of RichRap's design (Fig. 3E, 3 G) were removed and replaced with a filleted, steep wall to reduce a non-productive build-up of powder build material within the funnel (Fig. 3F, 3 H). These three key modifications allowed powder build material to be efficiently directed into contact with the auger, allowing improved powder feed into the hot end.

2.3. Motor and gearing system modifications for PME

Although the redesigned funnel delivered powder build material into the hot end, the extrusion was limited to a globule of material around the nozzle. To overcome this deficiency, the torque on the auger was increased. The NEMA 17 motor was replaced with a larger stepper motor capable of producing 0.88 N-m of torque and the gearing ratio was adjusted to generate a 4X torque ratio instead of the original 2X torque ratio (see the Gearing Ratio Calculations section in the Supporting Information for additional details). Combined with an increase in torque, increasing the diameter of the hot end nozzle to 0.8 mm from 0.4 mm allowed for consistent extrusion.

2.4. Addition and modification of an inlet

Despite constant extrusion, a buildup of powder material between the funnel and hot end was observed. This buildup of powder material exerted sufficient pressure to the top of the RPWHE and screws holding the hot end in place to split the funnel along the 3D printed layers adjacent to the screws. Although a funnel machined out of aluminum would help avoid this problem, the associated costs of machining this complex funnel part would create a large barrier to widespread adoption of powder melt extrusion. Therefore, to keep powder melt extrusion inexpensive and obtainable, the connection between the funnel and hot end was modified to consist of a short (5 mm) inlet from the funnel into the hot end (Fig. 3D) in order to reduce the observed pressure buildup.

The addition of the inlet extended successful extrusion to minutes from seconds, although the uniformity of the extruded material volume remained inconsistent. Therefore, it was hypothesized that the lack of consistency of the material feed into the hot end resulted in inconsistent extrusion. To facilitate a more consistent build material feed, the dimensions of the designed parts for the printer head and how they translated to the printed dimensions of the printer head parts were

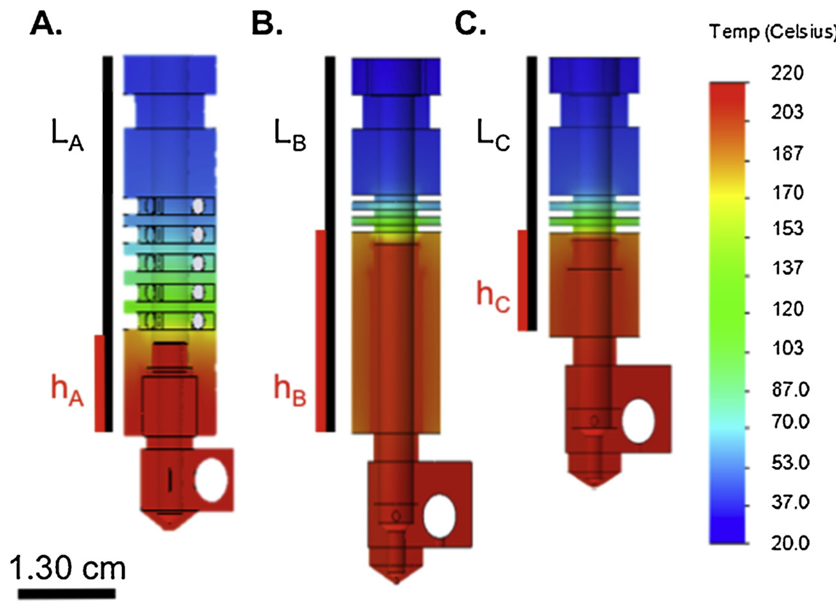

Fig. 5. Heat map portrayals of thermal simulations for the different hot ends surveyed for the PME printer. RPWHE length (L_A) = 5.08 cm, RPWHE metal insert length (h_A) = 1.30 cm, LTHE length (L_B) = 5.08 cm, LTHE metal insert length (h_B) = 2.56 cm, STHE length (L_C) = 3.69 cm, STHE metal insert length (h_C) = 1.30 cm.

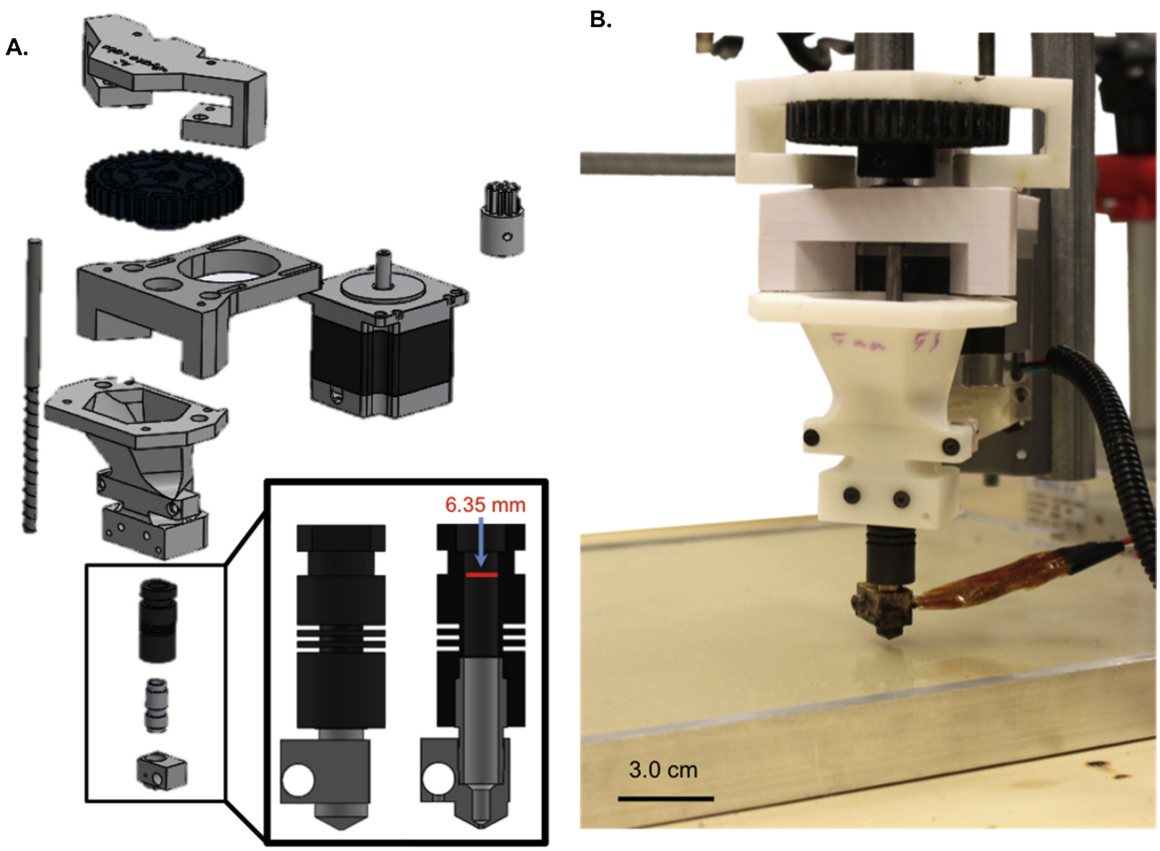

Fig. 6. A diagram of the exploded assembly computer model with an inset including a cross-sectional view of the STHE (A.) and a photograph of the assembled final version of the PME printer head (B).

examined. This comparison was done to determine how the exact dimensions of the printer head affected the feed of the powder into the hot end. The dimensions of the printed parts were found to be 0.2–1.0 % different than the design due to the extrudate contractions after printing [37]. Initially, it was assumed that these material contractions would not significantly affect the printer performance, especially as they would affect the funnel dimensions rather than the hot end. However, the contractions of the material comprising the funnel inlet that allowed the auger to transport material into the hot end were especially damaging to the extrusion performance by reducing the space between the auger and the sidewalls increasing the potential for the auger to rub against the sidewalls, as well as, reducing the amount of powder build material able to reach the hot end at one time. By accounting for the material contractions, the auger hole diameter was

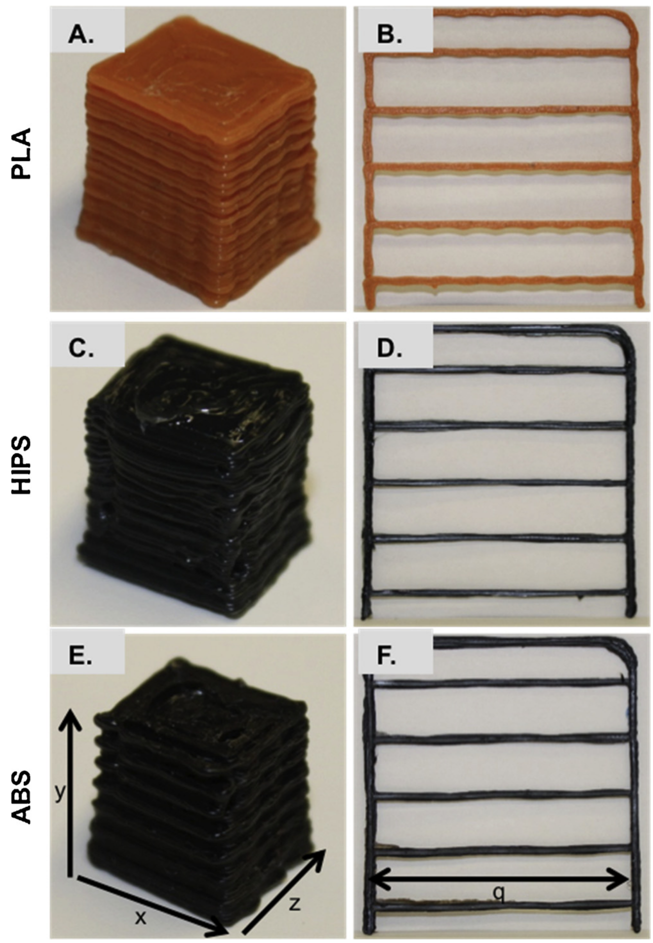

Fig. 7. Photographs of prints *via* Powder Melt Extrusion (PME) of all 3 materials (PLA cube (A.), PLA rail (B.), HIPS cube (C.), HIPS rail (D.), ABS cube (E.), ABS rail (F.)). X, Y, Z = 1.0 cm: q = 6.0 cm.

printed to the appropriate size that promotes minimal contact between the auger and the sidewalls and allows for a more consistent build material feed into the hot end, which leads to improved extrusion uniformity.

With a redesigned funnel, greater torque limit, and more accurate design tolerances, the fabricated printer head obtained constant powder melt extrusion (Fig. 4); however, during extrusion, a build material obstruction in the hot end formed approximately a few millimeters below the funnel inlet. This build material obstruction was a product of heat creep. Heat creep is the process of heat diffusion from the nozzle past the heat fins in the hot end, and as a result of the heat diffusion, the powder build material softens prematurely, and the increased viscosity of the coalescing powder granules clogs the hot end prohibiting any further extrusion or completion of 3D prints. Therefore, the most influential modification to the design of the printer head to enable PME printing was the design of the hot end to manage heat diffusion and minimize build material obstructions (Fig. 5).

2.5. Hot end investigation and optimization

To investigate the heat transfer within the hot end of the original RPWHE design, Solidworks Thermal Analysis software was used to simulate the thermal heat flow (Fig. 5A, heater cartridge reference temperature = 220 °C). This simulation revealed a large intermediate heat region (53 °C – 170 °C) attributed to heat creep through the hot end. To limit the intermediate heat region within the hot end, two more hot ends were designed (Figs. 5B and 5C). The first design, a long travel hot end (LTHE), was the same length as the RPWHE (Fig. 5, $L_A = L_B$) but contained two annular heat fins to better confine heat flow and a longer metal insert into the hot end to bring higher temperatures farther into the hot end (Fig. 5, $h_A < h_B$). The LTHE design reduced the temperature of the medium heat region (50 °C – 170 °C) in comparison to the RPWHE. However, due to an increased amount of softened build material around the auger, using the LTHE resulted in increased lateral motion of the hot end during the print, reducing the straightness of the printed lines and the overall print quality. To overcome this challenge of a long moment arm, a short travel hot end (STHE) (Fig. 5C) was designed (see Figure S6 and the Moment Arm Calculations section in the Supporting Information). The STHE contains the same heat fin design as the LTHE, creating a sharp transition between cold powder and melted plastic; however, the STHE is shorter than both the RPWHE and the LTHE (Fig. 5) to minimize lateral motion of the hot end during the print as a result of a smaller moment arm. The reduction of the distance between the nozzle and the funnel in the STHE likely reduced the lateral movement experienced during printing leading to increased print quality as evidenced by more uniform print lines with minimal side to side travel observed qualitatively from a printed line (Figure S7). Overall, minimizing heat creep allowed for improved extrusion while the STHE increased the uniformity of the printed layers resulting in the best overall performance.

With an improved funnel and the STHE incorporated into the printer, the material capabilities of the PME printer head were evaluated (Fig. 6). The print temperature of PLA powder, high impact polystyrene (HIPS) powder, and acrylonitrile butadiene styrene (ABS) powder build material was optimized by systematically tuning the temperature of the hot end and observing extrusion consistency as well as the connectivity of printed lines at defined 5 °C temperature intervals starting at 100 °C + glass transition temperature or the melting point

Table 1
Measured dimensions and calculated densities for each one of the cubes printed by FFF and PME with percent error from the theoretical values included.

Build Material	Print Technique	Cube Length (cm) [*% error*]	Cube Width (cm) [*% error*]	Cube Height (cm) [*% error*]	Cube Volume (cm^3) [*% error*]	Cube Mass (g) [*% error*]	Density of Printed Cube (g/cm^3) [*% error*]	Density of Non-Printed Filament (g/cm^3)
PLA	FFF	0.969 [3.10]	0.960 [4.00]	1.03 [3.00]	0.962 [3.80]	0.683 [44.5]	0.710 [42.3]	1.23
	PME	0.939 [6.10]	1.02 [2.00]	0.939 [6.10]	0.900 [10.0]	0.971 [21.1]	1.08 [12.2]	
HIPS	FFF	0.986 [1.40]	0.976 [2.40]	1.01 [1.00]	0.967 [3.30]	0.529 [48.6]	0.547 [46.9]	1.03
	PME	0.885 [11.5]	1.00 [0.00]	0.882 [11.8]	0.782 [21.8]	0.647 [37.2]	0.827 [19.7]	
ABS	FFF	0.978 [2.20]	0.976 [2.40]	0.995 [0.50]	0.949 [5.10]	0.511 [54.8]	0.538 [52.4]	1.13
	PME	0.846 [15.4]	0.993 [0.70]	0.960 [4.00]	0.806 [19.4]	0.652 [42.3]	0.809 [28.4]	

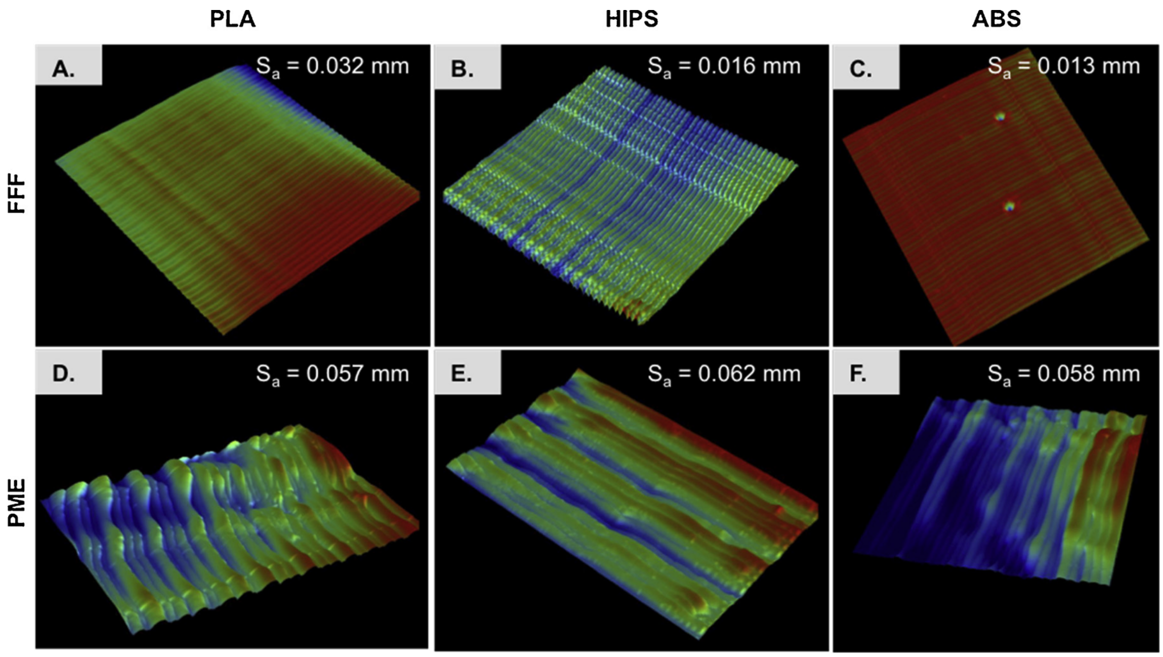

Fig. 8. Three-Dimensional renderings of profilometer generated surface maps for FFF printed parts out of PLA (A.), HIPS (B.), and ABS (C.), as well as, for PME printed parts out of PLA (D.), HIPS (E.), and ABS (F.) Red is indicative of a peak (+) above the designated 0 point (green) while blue is indicative of a valley (-) below the designated 0 point. The range of the measurement is ± 500 microns around the 0 point (For interpretation of the references to colour in this figure legend, the reader is referred to the web version of this article).

(see Table S3 for additional details). Operating at the optimized printing temperatures for each powder build material, the final version of the PME printer head was able to successfully complete 3D prints.

3. Print results and discussion

The print performance of the final PME design (Fig. 6) was first compared by qualitatively observing the differences in print quality to that of a commercially available bench-top FFF printer, the FlashForge Creator Pro. The comparison in print quality between the two methods of printing demonstrates the promise of the PME technique (Fig. 7 and S31). A small cube (1 cm^3) was printed using both the PME (Fig. 7A, 7C, 7E) and the FFF printers. In addition, a 2D ladder object was printed to isolate the consistency and quality of the print layers (Fig. 7B, 7D, 7 F). Although both techniques produced 3D objects, the FFF cube and ladder prints had higher print quality than the PME prints based on the layer uniformity with fewer print defects or lateral motion within layers (Fig. 7 and S31).

The lower print quality demonstrated here by the PME technique is due to inconsistent extrusion and lower print resolution. For PME, the extrusion method requires an auger to continually supply a steady stream of melted plastic to the nozzle to be extruded. However, due to a regular, drop-like appearance in the ladder prints (Fig. 7), it can be inferred that this characteristic is due to a less uniform feed of the build material to the nozzle compared to that of FFF printers. The print resolution of the PME technique is significantly lower than the print resolution of the FFF printer due to the differences in overall printer design and in nozzle diameter. In particular, the FlashForge Creator Pro has better X–Y resolution (0.4 mm) and Z-layer height (0.18 mm) [38] than the PME (X–Y resolution = 0.8 mm, Z-layer height = 0.1 mm), leading to higher quality prints by the FlashForge Creator Pro.

3.1. Print dimensions

Table 1 provides quantitative measurements of the dimensions of each of the cubes printed in Fig. 7 and Figure S31. It is apparent that the dimensions of the PME printed cubes are consistently shorter than the target dimension of 1 cm. In the case of the PME printed ABS cube, the cube length falls short of 1 cm by 1.5 mm. The dimensions of the FFF printed cubes are also shorter than 1 cm, but not by more than 0.5 mm. These quantitative measurements further validate the qualitatively observed differences between the print qualities of the cubes discussed in Section 3.

Although the dimensions of the PME cubes are consistently shorter than those of the FFF cubes, the densities of the PME cubes are more similar to that of the density of a 100% infilled cube of the respective material than those of the FFF cubes. The density of a 100% infilled cube was estimated by calculating the density of the parent filament [39]. The FFF cubes are consistently close to half of the desired density, which demonstrates that although the print pattern follows the 100% infill pattern, there are separations between the layers and not much layer overlap. In stark contrast, the PME cubes are closer to the desired 100% density, which demonstrates that the PME layers overlap more than that of the FFF layers to reduce the overall amount of void space within the print. The overlap of the PME layers compared to that of the FFF layers is another result of the inconsistent build material feed of the PME printing process.

3.2. Print surface roughness

To help quantify the print quality and the inconsistent layers produced with PME versus those produced with FFF beyond the dimensional analysis, surface roughness measurements (S_a) were taken using a profilometer. The three dimensional surface maps of one side of each cube are shown in Fig. 8. The PME cube surfaces are more heterogeneous compared to those of the FFF cube surfaces. Therefore, this surface variability is reflected in the S_a -values for each cube, which are 0.032 mm for the FFF printed PLA cube (Figure 8A), 0.057 mm for the PME printed PLA cube (Figure 8D), 0.016 mm for the FFF printed HIPS cube (Figure 8B), 0.062 mm for the PME printed HIPS cube (Figure 8E), 0.013 mm for the FFF printed ABS cube (Fig. 8C), and 0.058 mm for the PME printed ABS cube (Fig. 8F).

In every material printed, the surface roughness values of the PME printed cubes are more than those of the FFF printed cubes. This further

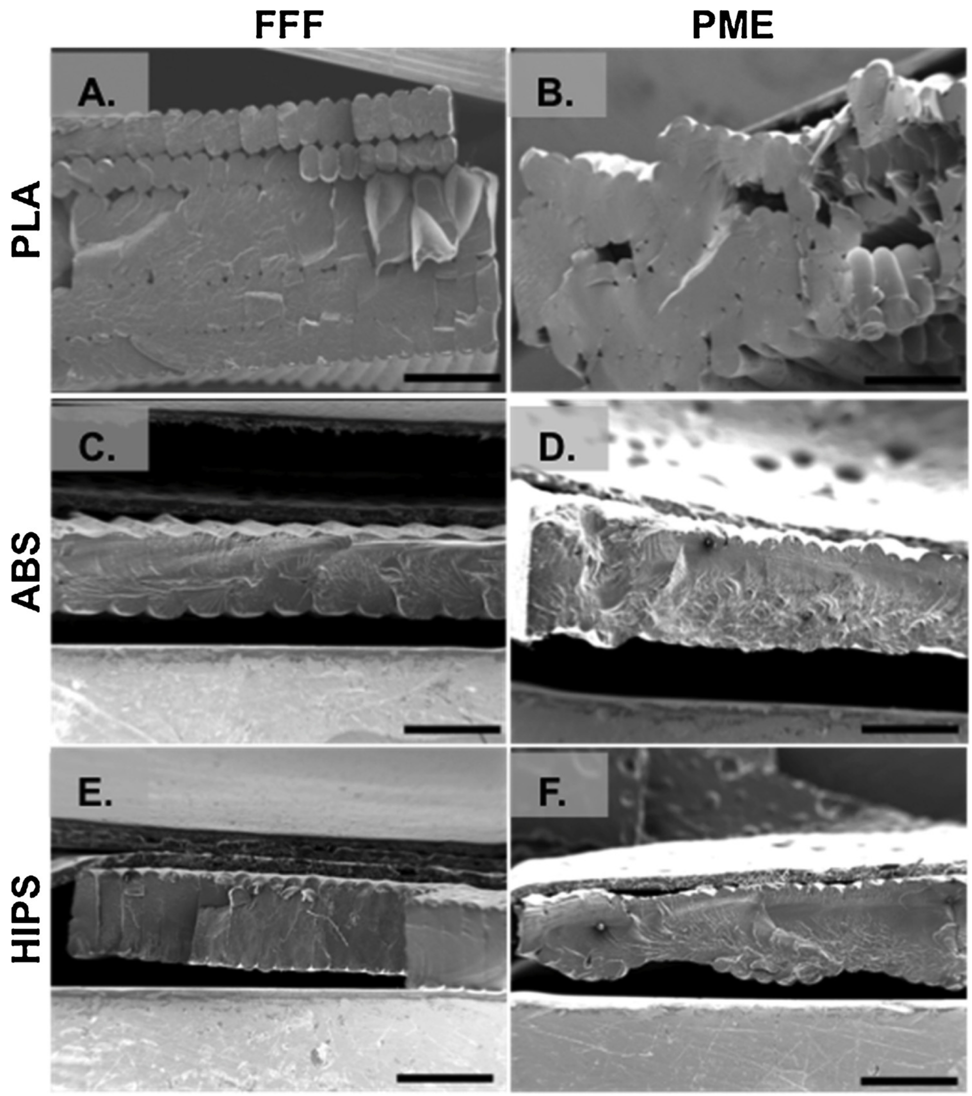

Fig. 9. SEM images of cross-sections of freeze-fractured 3D printed tabs from of PLA *via* the FFF printer (A.) and the PME printer (B.), of HIPS *via* the FFF printer (C.) and the PME printer (D.), of ABS *via* the FFF printer (E.) and the PME printer (F.). Scale bar = 1.0 mm.

verifies that the print quality of the PME printed parts is not as precise as the FFF printed parts due to printed layer inconsistencies produced by inconsistent build material extrusion in PME.

3.3. Print microstructures

To look closer at the difference in the layer consistency between the PME and FFF print methods, scanning electron microscopy (SEM) micrographs were taken of freeze-fractured tabs produced by each print method (Fig. 9). The PME printed layers were observed to either blend together or have gaps between adjacent layers due to uneven extrusion, whereas, the FFF printed layers are distinguishable from each other and contain minimal amounts of irregular gaps between adjacent layers. These visualized defects of the PME printed tabs provide insight into the internal structures of the 3D printed objects and suggest that microscopic defects due to less uniform extrusion give rise to poorer macroscopic print resolution compared with the FFF prints.

3.4. Bulk tensile properties of 3D printed objects

Before bulk tensile properties were analyzed, the integrity of the PME extrudate was verified to explore if degradation of the build material occurred during the powder preparation process. The powder preparation process involved taking FFF prints and mechanically grinding them into a powder form (see Materials and Methods in the Supporting Information for additional details). Comparison of the viscoelastic properties of the rectangular tabs printed by PME (average width = 10.9 mm, average thickness = 1.66 mm) and FFF (average width = 12.9 mm, average thickness = 1.00 mm) in each material (PLA, HIPS, and ABS) on a dynamic mechanical analyzer (DMA) revealed that printing using the PME process did not affect the material performance of parts relative to those printed by FFF (Figure S26). Specifically, the average storage moduli (E’) of tabs from each method directly are nearly identical under tension for each material. Further, as expected, the glass transition temperature marked by the alpha transition of the storage modulus trace is systematically greater than the temperature determined by DSC in every case (Figure S26 and Table S3).

To compare the mechanical properties of parts printed by the different methods, the bulk tensile properties of ASTM standard type 5 dog bones printed in PLA by both PME and FFF print methods were tested with the print layers oriented parallel to the direction of the tensile force (Fig. 10). The print temperatures of the ABS and HIPS materials were too high to complete full dog bone prints without destroying the inside of the PEEK tube of the STHE, and therefore, these objects could not be printed with the current set up. Testing the dog bones with the print layers oriented parallel to the direction of the tensile force

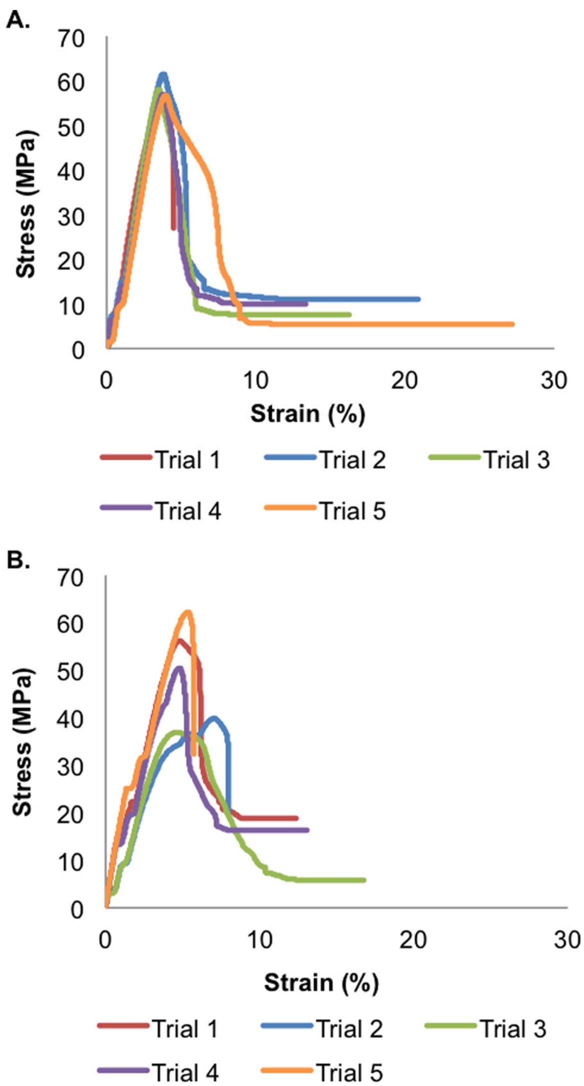

Fig. 10. Plots of the stress-strain relationship for the printed PLA dog-bones by FFF (A.) and PME (B.) under tension.

reduced the amount of extraneous variables such as layer adhesion or number of layers present [39–41]. Although data beyond the initial failure is insignificant for the purpose of this study, the triangular shapes of the stress-strain traces can be explained by considering the print orientation of the dog bones. As tension is applied parallel to each printed strand, each strand breaks individually. Thus, when one strand in the print breaks, the bulk stress measured lessens, but the strain continues until every strand is broken.

Analysis of the stress-strain curves for dog bones prepared using each printing method revealed that the tensile properties of the tabs were affected depending on the print technique (Fig. 10). Less variation of the average tensile strength values between samples of the FFF printed tabs (57.7 ± 2.31 MPa) (Fig. 10A) than that of the PME printed tabs (49.2 ± 10.7 MPa) was observed (Fig. 10B). Furthermore, the average Young's Modulus values exhibited by the FFF printed tabs (2160 ± 179 MPa) were more consistent (Fig. 10A) than those exhibited by the PME printed tabs (1620 ± 375 MPa) (Fig. 10B). The minimal variation of the FFF prints' tensile properties is not surprising after observing the layer uniformity within the SEM micrographs (Fig. 9). Additionally, the inconsistency of the PME prints' tensile properties is not surprising considering the lack of uniformity between layers within the PME prints as observed in the SEM micrographs (Fig. 9). Therefore, PME shows promise to be used as a viable 3D printing technique, however, to realize PME as an industrially viable printing option comparable to the FFF technique, further optimization and analysis of the PME print parameters and design will be needed.

4. Conclusions

A bench-top PME printer head was developed and tested. Each part of the RRUPE printer head was systematically investigated and modified to gain a fundamental understanding of the principles needed to fabricate a PME printer head. The final version of the PME printer head is able to successfully 3D print from a variety of thermoplastic powder build materials (PLA, HIPS, ABS). Printing by PME was also shown to minimally affect the viscoelastic properties of the material when compared to those of the FFF printed parts. However, the inconsistencies of the PME printed layers shown by dimensional analysis, surface roughness measurements, and SEM micrographs did present variable tensile properties in the printed parts when compared to the more consistent layers produced from the FFF print method. The layer inconsistencies of PME printed parts are likely a result of uneven powder melt extrusion which presents further challenges in achieving consistent material flow during extrusion, as well as being able to enhance PME print resolution. PME print methods have the potential to reduce the time needed for the processing of 3D printing build materials, presenting the opportunity to provide a platform on which it is possible to rapidly prototype a myriad of thermoplastic materials for 3D printing.

Declaration of Competing Interest

We confirm that there are no conflicts of interest related to this manuscript

Acknowledgements

We would like to acknowledge the Colorado State University, the National Science Foundation (CMMI-1634941) and the National Institute of General Medical Sciences of the National Institutes of Health under Award Number R35GM119702 for funding. The content is solely the responsibility of the authors and does not necessarily represent the official views of the National Institutes of Health. We thank Prof. Mark A Ganter, Prof. Andrew J. Boydston, and Johanna J. Schwartz from the University of Washington for the gift of the MPCNC printer and help with its assembly. We would also like to thank Brian Reifsnyder of Reifsnyder Precision Works for machining expertise and helpful discussions. Further, the authors would like to thank Pat McCurdy for his SEM expertise, as well as Kyle Foster and Max Kudisch for enlightening discussions and photography contributions.

Appendix A. Supplementary data

Supplementary material related to this article can be found, in the online version, at doi:https://doi.org/10.1016/j.addma.2019.100811.

References

[1] N. Jones, Science in three dimensions: the print revolution, Nature 487 (2012) 22–23.
[2] J.-P. Kruth, M.C. Leu, T. Nakagawa, Progress in additive manufacturing and rapid prototyping, CIRP Ann. Manuf. Technol. 47 (1998) 525–540.
[3] B.P. Connor, G.P. Manogharan, A.N. Martof, L.M. Rodomsky, C.M. Rodomsky, D.C. Jordan, J.W. Limperos, Making sense of 3-D printing: creating a map of additive manufacturing products and services, Addit. Manuf. 1–4 (2014) 64–76.
[4] Y. Huang, M.C. Leu, J. Mazumder, A. Donmez, Additive manufacturing: current state, future potential, gaps and needs, and recommendations, J. Manuf. Sci. Eng. 137 (2015) 014001-1–014001-10.
[5] I. Campbell, D. Bourell, I. Gibson, Additive manufacturing: rapid prototyping comes of age, Rapid Prototyp. J. 18/4 (2012) 255–258.
[6] K.V. Wong, A. Hernandez, A review of additive manufacturing, ISRN Mech. Eng. 10 (2012) 208760.
[7] J.R. Tumbleston, D. Shirvanyants, N. Ermoshkin, R. Janusziewicz, A.R. Johnson,

D. Kelly, K. Chen, R. Pinschmidt, J.P. Rolland, A. Ermoshkin, E.T. Samulski, J.M. DeSimone, Continuous liquid interface production of 3D objects, Science 347 (2015) 1349–1352.
[8] H. Yin, Y. Ding, Y. Zhai, W. Tan, X. Yin, Orthogonal programming of heterogeneous micro-mechano-Environments and geometries in three-dimensional bio-stereo-lithography, Nat. Comm. 9 (2018) 4096.
[9] J.-P. Kruth, P. Mercelis, J. Van Vaerenbergh, Binding mechanisms in selective laser sintering and selective laser melting, Rapid Prototyp. J. 11/1 (2005) 26–36.
[10] N.D. Dolinski, Z.A. Page, E.B. Callaway, F. Eisenreich, R.V. Garcia, R. Chavez, D.P. Bothman, S. Hecht, F.W. Zok, C.J. Hawker, Solution mask liquid lithography (SMaLL) for one-step, multimaterial 3D printing, Adv. Mater. 30 (2018) 1800364.
[11] S.S. Crump, Apparatus and Method for Creating Three-Dimensional Objects, US Patent 5121329, Priority Date October 30, 1989 (1992).
[12] E. MacDonald, R. Wicker, Multiprocess 3D printing for increasing component functionality, Science 353 (2016) aaf2093.
[13] G.I. Peterson, M.B. Larsen, M.A. Ganter, D.W. Storti, A.J. Boydston, 3D-printed mechanochromic materials, ACS Appl. Mater. Interfaces 7 (2015) 577–583.
[14] O. Rios, W. Carter, B. Post, P. Lloyd, D. Fenn, C. Kutchko, R. Rock, K. Olson, B. Compton, 3D printing via ambient reactive extrusion, Mater. Today Comm. 15 (2018) 333–336.
[15] ISO/ASTM 52900, Standard Terminology for Additive Manufacturing – General Principles – Terminology, (2015).
[16] B.N. Turner, R. Strong, S.A. Gold, A review of melt extrusion additive manufacturing processes: I. Process design and modeling, Rapid Prototyp. J. 20/3 (2014) 192–204.
[17] B.N. Turner, S.A. Gold, A review of melt extrusion additive manufacturing processes: II. materials, dimensional accuracy, and surface roughness, Rapid Prototyp. J. 21/3 (2015) 250–261.
[18] T.A. Osswald, J. Puentes, J. Kattinger, Fused filament fabrication melting model, Addit. Manuf. 22 (2018) 51–59.
[19] M. Hofmann, 3D printing gets a boost and opportunities with polymer materials, ACS Macro Lett. 3 (2014) 382–386.
[20] J.W. Stansbury, M.J. Idacavage, 3D printing with polymers: challenges among expanding options and opportunities, Dent. Mater. 32 (2016) 54–64.
[21] S.C. Ligon, R. Liska, J. Stampfl, M. Gurr, R. Mulhaupt, Polymers for 3D printing and customized additive manufacturing, Chem. Rev. 117/15 (2017) 10212–10290.
[22] D. Robertson, C.M. Shemelya, E. MacDonald, R. Wicker, Expanding the applicability of FDM-type technologies through materials development, Rapid Prototyp. J. 21/2 (2015) 137–143.
[23] B.M. Boyle, T.A. French, R.M. Pearson, B.G. McCarthy, G.M. Miyake, Structural color for additive manufacturing: 3D-Printed photonic crystals from block copolymers, ACS Nano 11 (2017) 3052–3058.
[24] F. Ning, W. Cong, J. Qiu, J. Wei, S. Wang, Additive manufacturing of carbon Fiber reinforced thermoplastic composites using fused deposition modeling, Compos. Part B Eng. 80 (2015) 369–378.
[25] D. Espalin, D.W. Muse, E. MacDonald, R.B. Wicker, 3D printing multifunctionality: structures with electronics, Int J Adv Manuf Technol 72 (2014) 963–978.
[26] S.E. Bakarich, R. Gorkin III, M. Panhuis, G.M. Spinks, Three-dimensional printing Fiber reinforced hydrogel composites, ACS Appl. Mater. Interfaces 6 (2014) 15998–16006.
[27] A.J. Boydston, B. Cao, A. Nelson, R.J. Ono, A. Saha, J.J. Schwartz, C.J. Thrashert, Additive manufacturing with stimuli-responsive materials, J. Mater. Chem. A Mater. Energy Sustain. 6 (2018) 20621.
[28] N. Holshouser, L. Palas, L. Kunc, R. Lloyd, D. Blue, D. Peter, Out of bounds additive manufacturing, Advanced Materials and Processes (AM&P) 171 (3) (2013) 15–17.
[29] C.E. Duty, V. Kunc, B. Compton, B. Post, D. Erdman, R. Smith, R. Lind, P. Lloyd, L. Love, Structure and mechanical behavior of big area additive manufacturing (BAAM) materials, Rapid Prototyp. J. 23/1 (2017) 181–189.
[30] V. Kishore, C. Ajinjeru, A. Nycz, B. Post, J. Lindahl, V. Kunc, C. Duty, Infrared preheating to improve interlayer strength of big area additive manufacturing (BAAM) components, Addit. Manuf. 14 (2017) 7–12.
[31] Titan 3D Robotics, The Atlas: Purpose Built, Production Ready, (2016) (Accessed 24 January, 2019), http://www.titan3drobotics.com/atlas/.
[32] Direct3D, Direct3D: Pellet Extrusion Made Possible (Accessed 24 January, 2019), https://www.direct3d.it/.
[33] Rich Rap Blogspot, Reprap Development and Further Adventures in DIY 3D Printing: Quest for a Universal Pellet Extruder for 3D Printing, (2014) https://richrap.blogspot.com/2014/12/no-more-filament-quest-for-universal.html.
[34] N. Volpato, D. Kretschek, J.A. Foggiatto, C.M. Gomez da Silva Cruz, Experimental analysis of an extrusion system for additive manufacturing based on polymer pellets, Int. J. Adv. Manuf. Technol. 81 (2015) 1519–1531.
[35] V1 Engineering, The MPCNC Assembly: Before You Begin, (2018) (accessed 24 January, 2019), https://www.v1engineering.com/assembly/.
[36] L.L.C. Hotends, Hotends About Us, (2011) (Accessed 24 January, 2019), https://www.hotends.com/aboutus.
[37] 3D Hubs, Basic Manufacturing Principles: Dimensional Accuracy of 3D Printed Parts, (2019) (Accessed 24 January, 2019), https://www.3dhubs.com/knowledge-base/dimensional-accuracy-3d-printed-parts#fdm.
[38] FlashForge 3D Printer, Creator Pro 3D Printer Overview. http://www.flashforge.com/creator-pro-3d-printer/, 2012-2018. (Accessed 24 January 2019).
[39] C.M. Shemelya, A. Riviera, A.T. Perez, C. Rocha, M. Liang, X. Yu, C. Kief, D. Alexander, J. Stegeman, H. Xin, R.B. Wicker, E. Macdonald, D.A. Roberson, Mechanical, Electromagnetic, and X-ray Shielding Characterization of a 3D Printable Tungsten-Polycarbonate Polymer Matrix Composite for Space-Based Applications, J. Korean Inst. Electr. Electron. Mater. Eng. 44 (2015) 2598–2607.
[40] A.R. Torrado Perez, D.A. Roberson, R.B. Wicker, J. Fail, Anal. and Preven. 14 (2014) 343–353.
[41] C. Rocha, A. Torrado-Perez, D.A. Roberson, C. Shemelya, E. MacDonald, R. Wicker, J. Mater. Res. 29 (2014) 1859–1866.